International Journal of Pressure Vessels and Piping 212 (2024) 105315

Contents lists available at ScienceDirect

International Journal of Pressure Vessels and Piping

journal homepage: www.elsevier.com/locate/ijpvp

Impact of stacking sequence on burst pressure in glass/epoxy Type IV composite overwrapped pressure vessels for CNG storage

Lucas L. Agne [a], José Humberto S. Almeida Jr [b,*], Sandro C. Amico [c], Maikson L.P. Tonatto [a]

[a] Group on Mechanics of Materials and Structures – GMEC, Federal University of Santa Maria, Cachoeira do Sul, Brazil
[b] Department of Mechanical Engineering, LUT University, Lappeenranta, Finland
[c] PPGE3M/PROMEC, Federal University of Rio Grande do Sul, Porto Alegre, Brazil

ARTICLE INFO

Keywords:
Composite pressure vessel
Finite element analysis
Burst pressure
CNG storage
Filament winding

ABSTRACT

The shift from metallic to composite pressure vessels for storing compressed natural gas (CNG) is driven by the goal of reducing environmental impact by using lighter higher-performing structures. This work focuses on enhancing the internal pressure strength of a type IV composite overwrapped pressure vessel (COPV) by optimising the stacking sequence of the overwrapping composite layers. Parametric finite element (FE) models are developed to reveal symmetry effects. In these models, both the thickness build-up and fibre angle variation at the turnaround zones are accurately modelled. Subsequently, the stacking sequence is optimised with the objective function of maximising burst strength. The parametric modelling demonstrates that representing the COPV as an axisymmetric continuum reduces computational costs in 5400× while yielding results comparable to full 3D continuum models. Experimental burst tests are carried out to validate the numerical predictions, and the difference in pressure between them is 12.6 %.

Abbreviations

3DC	3D continuum
3DS	3D shell
AC	Axisymmetric continuum
AS	Axisymmetric shell
COPV	Composite overwrapped pressure vessel
CNG	Compress natural gas
CNC	Computer numerical control
FE	Finite element
FW	Filament winding
IF	Failure index
Seq1, 2, 3, …21	Stacking sequence 1, 2, 3 … 21
Seq2_ref	Reference stacking sequence 2
Seq2_var1, 2, 3 and 4	Variations 1, 2, 3 and 4 of the reference stacking sequence 2
SG-A, B, C and D	Strain gauge A, B, C and D
RAM	Random access memory

1. Introduction

High-performance fibre-reinforced polymer composites play a crucial role in energy storage and transportation due to their very high strength-to-weight ratio compared to conventional material (e.g., steel), high corrosion resistance, design flexibility, long-term performance and high cost-effectiveness [1]. Modern mobility using cleaner and renewable fuel sources can mitigate the ever-growing climate issues. Yet increasingly lighter and stronger structures are needed to store large volumes of fuels under high pressure, allowing higher payload [2,3].

Current market solutions for CNG storage involve pressure vessels, known as types I, II, and III, which use metallic materials like steel. These well-established solutions are not as suitable for transportation due to the heavy weight of steel and its negative environmental impacts. Type IV, consisting of composite layers overwrapping a polymeric liner, also known as COPV, offers improved performance since the composite layers provide lightweight and strength, while the liner acts as a barrier to contain the fluid [4,5].

CNG is stored in compressed form in pressure vessels that operate at pressures within 20–25 MPa to offset its low energy density [6,7]. CNG fuel tanks were all metallic (type I) but issues related to weight and corrosion led to the development of tanks with composite reinforcement, which enhanced their commercial appeal [8]. Despite the development, high-pressure storage may lead to failure, posing significant risks related to vehicle damage and fatalities of the occupants, so CNG cylinders for vehicles must adhere to stringent safety standards [9].

* Corresponding author.
E-mail address: humberto.almeida@lut.fi (J.H.S. Almeida Jr).

https://doi.org/10.1016/j.ijpvp.2024.105315
Received 9 July 2024; Received in revised form 30 August 2024; Accepted 6 September 2024
Available online 7 September 2024
0308-0161/© 2024 The Authors. Published by Elsevier Ltd. This is an open access article under the CC BY license (http://creativecommons.org/licenses/by/4.0/).

Safety is paramount for structures that carry compressed gas. However, conducting experiments to test COPV under internal pressure is costly, and computational models appear as a cost-effective means to evaluate these structures. For instance, Sharma et al. [6] used the Tsai-Wu and Tsai-Hill failure criteria to numerically determine the burst pressure of a type IV cylinder for CNG storage, reaching 80.1 MPa, very close to the experimental value, 82.4 MPa. Failure prediction using equivalent stress was also employed to study COPV failure, as in Sharma et al. [10]. This involved a straightforward comparison between the working pressure, the resulting tensile stress in the fibre direction of the composite, and its strength. Sharma et al. [11] applied Tsai-Wu and Tsai-Hill failure criteria to determine the burst pressure of type III COPV for hydrogen storage, reaching 79.6 MPa, nearly the same as the experimental value (79.7 MPa).

Nebe et al. [12] studied the effect of the stacking sequence on laminate quality, structural deformation and burst pressure for a type IV COPV. Higher winding angles on outer layers increased the compaction of inner layers, leading to lower porosity and higher fibre content. Later, Nebe et al. [13] carried out an experimental and numerical study on a similar COPV under internal pressure and reported that the impact of circumferential ply drop locations on the burst pressure was heavily influenced by the stacking sequence, where sequences with circumferential layers and high-angle helical layers positioned as inner layers exhibited high sensitivity to any ply drop retraction. Conversely, for stacking sequences with circumferential layers and high-angle helical layers as outer layers, changes in burst performance were negligible. The difference in behaviour was attributed to the layer interfaces and the associated development of interlaminar damage. Hu et al. [14] investigated numerically and experimentally the dome of type IV COPV for hydrogen storage and concluded that the variations in dome shape can reduce the amount of composite material by 5.5 % without compromising the burst pressure.

From the literature review, it appears that computationally efficient finite element (FE) models to accurately simulate the performance of type IV COPV structures are not yet available, and it remains unclear how important is the stacking sequence on the burst pressure, and how helical and hoop layers can be most efficiently allocated. This paper aims to address these issues by parametrically modelling a type IV COPV with different symmetry and finite elements (axisymmetric shell, 3D shell, axisymmetric continuum, and 3D continuum), carrying out a sensitivity analysis of the geometric parameters, and finally optimising the stacking sequence focusing on higher burst resistance and lower weight.

2. Computational modelling

2.1. The FE modelling

The computational modelling of this work was carried out in Abaqus FE platform. The detailed design of the COPV, especially the winding angle variation and thickness build-up at the turnaround zones, is carried out in WoundSim, a dedicated software for filament-wound structures. The elastic properties also change locally according to the fibre angle and thickness of each finite element. The stacking sequence optimisation is performed in the same software, interfacing with Abaqus.

In this study, linear elastic analysis was used, therefore, the first-ply failure method is adopted. This may be deemed as a limitation, since progressive damage is not considered. Temperature variations and fatigue induced by loading/unloading cycles are also disregarded. And the composite model considers balanced layers, so for every +α orientation, there is a –α orientation.

The initial step in this study is to analyse the influence of symmetry and type of element in terms of computational cost. For that, linear-elastic FE models are built and the COPV is subjected to internal pressure. Firstly, axisymmetric and 3D with a quarter of symmetry models are developed for the parametric study, validating it based on the work of Kangal et al. [15]. The dimensions of the COPV used in this analysis are shown in Table 1.

For the parametric study, the elastic properties of polyamide 6 were used [14] to represent the liner. For the FE model validation study, the elastic properties reported by Kangal et al. [15] were employed. To simulate the experimental results, the tensile properties of high-density polyethylene have been experimentally measured., yielding Young's modulus (E) of 299.4 MPa and Poisson's ratio (ν) of 0.46. All material properties are presented in Appendix I.

For the prototype modelling, a quarter symmetry is applied, and boundary conditions and symmetry planes are shown in Fig. 1. A cylindrical coordinate system was used. A set is created on the outer contour of the liner geometry, which is then exported to WoundSim to design the composite overwrapping layers. A tie constraint with perfect contact is used between the external surface of the liner and the innermost composite layer. The pressure is applied to the inner surface of the liner.

The fibre path trajectory cannot be selected arbitrarily due to the inherent stability requirements of the FW process and the need for synchronisation between fibre trajectory and liner dimensions. The fibre path is directly influenced by the fibre slippage over the liner surface. An inappropriate fibre path leads to winding instability, deviations in fibre positioning, and high vibration levels in the winding equipment [16]. Considering that the inner radius of the liner is 160 mm in the cylindrical region of the COPV and 23 mm at the boss, fibre slippage was investigated using Clairaut's relation. The variation of non-slipping fibre angles with the liner radius R for the actual geometry is presented in Fig. 2. Based on that, ≈12° is considered here the lowest possible winding angle for this geometry.

Usually, before the FE modelling, netting analysis is employed in the design of COPV due to its simplicity and compliance with safety standards. For that, it is assumed that i) only the composite layers bear the load, and the fibres only bear the load along the fibre direction; ii) all fibres have the same strength; iii) the influence of the matrix and the fibre tensioning is disregarded. As output, the required fibre thicknesses at the cylindrical region of the COPV in the hoop, helical or polar directions are provided, which are useful to define the number of composite layers and/or tow bandwidth [6].

The initial thickness estimate used for the hoop layers is given by:

$$t_{hoop} = \frac{PR\left(1 - \frac{tan(\alpha)^2}{2}\right)}{\sigma_H} \tag{1}$$

where P is the applied pressure (defined as 47 MPa), R is the radius at the cylindrical region, and σ_H is the hoop tensile strength.

The calculated thickness is 5.65 mm, which is rounded up to 6 mm and divided by the layer thickness (0.5 mm) resulting in a total of 12 hoop layers. Given that the number of helical layers equals the number of hoop ones, and considering that helical layers are twice as thick, the total composite thickness in the cylindrical region is 18 mm. The layers used in the stacking sequence can be checked in Table 2.

Definition of layer thickness as a function of the radius, based on the volume conservation method, is given by:

$$t_{(r)} = \frac{t_{tl} \bullet cos(\theta_{tl})}{cos(\theta_r)} \tag{2}$$

Table 1
Dimensions of the COPV used in different steps of the current study.

Parameter	Kangal et al. [15]	Parametric study and prototype
External radius, $R_e(mm)$	70	160
Dome length, $L_D(mm)$	78	126
Cylinder length, $L_C(mm)$	183	522.5
Cylinder thickness, $t_C(mm)$	4.5	10

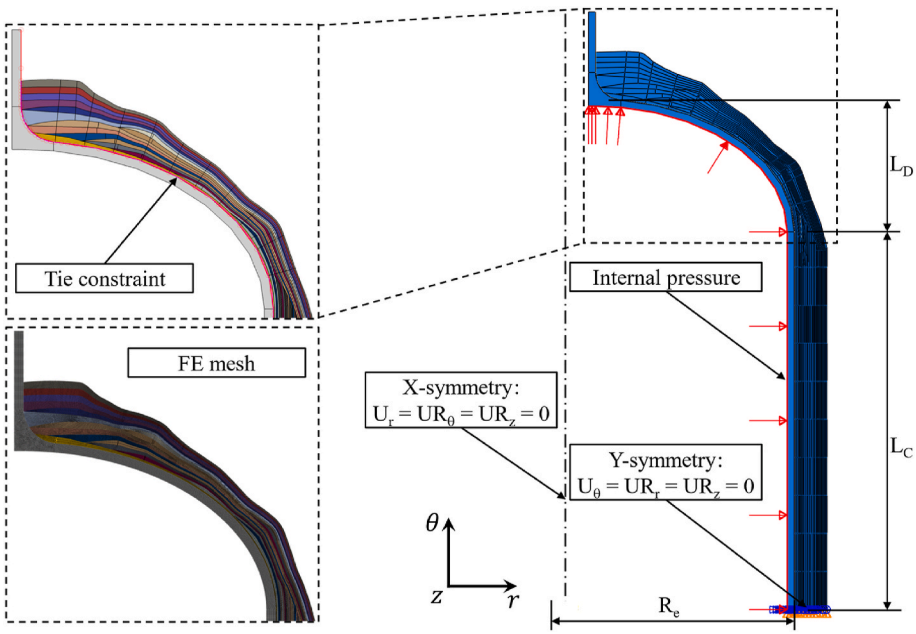

Fig. 1. Characteristics of the axisymmetric FE model used for the parametric models.

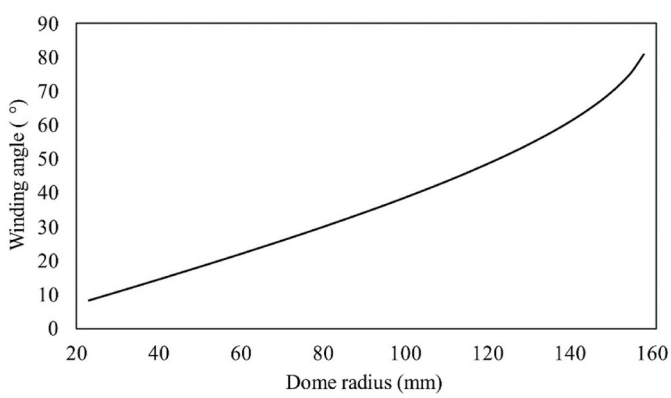

Fig. 2. Non-slipping angles using Clairaut's relation.

Table 2
Design of the number of layers to be used in the parametric study.

Parameter	Number of layers									
Winding angle (°)	12	18	24	30	36	42	48	54	60	89
Number of layers	4	1	1	1	1	1	1	1	1	12

where t_{tl} is the thickness on the tangential line, θ_{tl} is the winding angle on the tangential line, and θ_r is the winding angle calculated for the defined radius.

The helical layers are considered to follow a geodesic path, and its final deposition is automatically calculated, while for the hoop trajectory, the boundaries can be manually adjusted. A mesh convergence study is carried out to avoid a mesh-dependent behaviour, which is performed using the axisymmetric continuum model with CAX4 and CAX3 elements for the liner and composite, respectively. The converged FE mesh has 17,856 CAX4R elements and 23,688C3D8R elements.

Subsequently, the model with the generated composite layers is exported to Abaqus and attached to the liner using a tie constraint. Different FE mesh approaches were studied for the composite material: (i) in the axisymmetric shell model with 150 SAX1 elements; (ii) the Axisymmetric continuum model with 36,594 CAX8R and 53 CAX6 elements; (iii) the 3D shell model with 4500 S4R elements, and (iv) the 3D continuum model with 444,900C3D20R and 3500C3D15 elements. In shell models, the number of elements is significantly lower compared to their continuum counterparts of the same dimension due to fewer elements required in the thickness direction of the mesh. The four approaches are schematically depicted in Fig. 3.

2.2. Sensitivity analyses of geometric parameters

A comprehensive literature review identified various stacking sequences for COPV ([8,11,13–15,17–21]). Based on that, 21 stacking sequences (see Appendix II) were selected and considered in the current study aiming to obtain the highest burst pressure. The number of layers was adjusted to produce comparable thicknesses, reducing or adding the layers, and maintaining the repeating pattern of the sequences.

After selecting one stacking sequence, a sensitivity analysis was

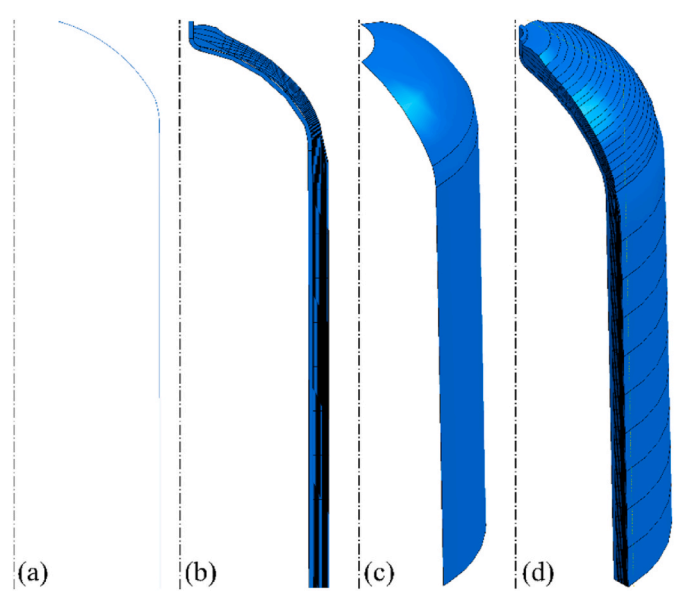

Fig. 3. Geometry of mesh (a) axisymmetric shell, (b) axisymmetric continuum, (c) 3D shell and (d) 3D continuum.

conducted. The hoop layers and the layer distribution in the thickness direction were kept constant, but the angles of the helical layers were varied at 10 % and 20 % increments above and below the reference value, corresponding to sequences Seq_var1, Seq_var2, Seq_var3, and Seq_var4, respectively. The layer configurations for each stacking sequence are detailed in Table 3.

3. Experimental

In the construction of the COPV, the liner is produced using the rotational moulding (rotomoulding) process to obtain the 3-D geometry. The thickness of the liner is ≈ 10 mm, with no significant variation along its length. Metallic boss and counter-boss are placed at the ends. A filament winding machine with four axes from CNC Technics is used to deposit the fibres, controlled and programmed with CADFIL software. Table 4 presents the orientation and number of layers in the manufacturing cylinder, with a bandwidth of 36 mm.

A prototype of the COPV using the Seq2_ref stacking sequence was produced, and subsequently cured at 100 °C for 6 h. Later, the COPV underwent hydrostatic testing based on the ISO 11439 standard. The test setup, shown in Fig. 4, positions the COPV horizontally in an isolated environment. Four strain gauges (SG) are positioned at both radial and axial directions of the COPV, as depicted in Fig. 4, named SG-A, SG-B, SG-C, and SG-D. The cylinder is filled with water, and the pressure is increased at a rate of 0.21 MPa/s. The maximum pressure reached before the structure fails is considered the burst pressure.

4. Results and discussion

4.1. Parametric FE modelling

Mesh selection is initially performed with a mesh convergence study for the two models, axisymmetric continuum and 3D continuum. The maximum normalised stress in the fibre direction as a function of the number of elements is shown in Fig. 5a-b for both models, respectively. The two dashed lines represent a ±1 % difference from the maximum value (denser mesh). Results within these limits are considered converged. Therefore, for the axisymmetric models, 400–500 elements were used in the contour of the cylindrical region and dome. In the 3D models, 150–200 elements were used in the cylindrical region and dome, and 50 elements in the revolution. The selected meshes are highlighted in the graphs. The meshes selected for the continuum models are also adopted for the shell-type models.

The influence of the type of model was studied by examining the stresses in the first hoop and helical layers under an internal pressure of 30 MPa, which were the most stressed hoop and helical layers of all models. Fig. 6 shows the normalised stress (with the maximum stress value obtained in the numerical analysis) in the fibre direction along its path on the mandrel contour. The hoop layers exhibit similar stress along their length, except for the axisymmetric shell (AS), which shows lower values. This can be attributed to the simplification of the model, resulting in reduced stresses. In the helical layers, the stresses for axisymmetric continuum (AC) and 3D continuum (3DC) models are nearly identical, and this is also true for axisymmetric shell (AS) and 3D shell (3DS) models. However, the shell models exhibit lower stresses in the dome region compared to the continuum models. This may be due to the greater thickness in the dome region, as the shell models do not account for deformation in the thickness direction, which can affect the results in this region.

The type of FE model also impacts computational performance. The numerical modelling and simulation on a workstation with 12 processing cores and 96 GB of RAM took 65 s for the axisymmetric shell model but only 20 s for the axisymmetric continuum model, despite having more elements than the shell models. The 3D shell model took 81 s, and the 3D continuum model was the slowest, with 7283 s. Comparing the two continuum meshes, the 3D model required 2 h, while the 2D model took only 20 s, yet both produced similar results.

Thus, the axisymmetric continuum model demonstrated superior computational performance and produced results comparable to the more complex 3D continuum model, being more suitable for simulating the burst pressure of the COPV. The 3D models may be better fitted for simulations involving non-symmetrical loads, such as the 45° drop test required by certain standards. Shell models are appropriate for structures with low thickness relative to their length. The axisymmetric continuum mesh is frequently employed in the literature for numerical models subjected to internal pressure and for burst pressure analysis [5, 14,22–25].

Table 3
Stacking sequences used for the sensitivity analysis.

Name	Stacking sequence
Seq2_ref	[±12/88/±12/±42/88_3/±35/±30/±23/88_3/±18/±12/88_3/±42/88_3/±35/±30/±23/88_3/±18_2/±12/88_3]
Seq2_var1	[±13/88/±13/±46/88_3/±39/±33/±25/88_3/±20/±13/88_3/±46/88_3/±39/±33/±25/88_3/±20_2/±13/88_3]
Seq2_var2	[±11/88/±11/±38/88_3/±32/±27/±21/88_3/±16/±11/88_3/±38/88_3/±32/±27/±21/88_3/±16_2/±11/88_3]
Seq2_var3	[±14/88/±14/±50/88_3/±42/±36/±28/88_3/±22/±14/88_3/±50/88_3/±42/±36/±28/88_3/±22_2/±14/88_3]
Seq2_var4	[±10/88/±10/±34/88_3/±28/±24/±18/88_3/±14/±10/88_3/±34/88_3/±28/±24/±18/88_3/±14_2/±10/88_3]

Table 4
Design of the number of layers to be used in the prototype.

Parameter	Number of layers						
Winding angle (°)	±12	±18	±23	±30	±35	±42	88
Number of layers	4	3	2	2	2	2	19

4.2. Comparing the FE model with literature results

The COPV in the work by Kangal et al. [15] was employed to validate the modelling methodology used in the current work. This included verifying the first ply failure criteria and comparing the numerical deformation with experimental values. Fig. 7 displays the pressure as a function of the strain gauge readings in the axial and hoop directions. The experimental strain gauge is located at the geometric centre of the COPV, on the outermost layer. The experimental curve from Kangal et al. [15] and the numerical curve of the present study are very similar in the linear region of the graph, up to ≈60 MPa. Above that, the numerical model shows relatively lower pressures.

For this model, the burst pressure was evaluated using several failure criteria: Tsai-Wu, Tsai-Hill, Hashin, maximum stress, and equivalent stress. Since the Hashin criterion is not available in the UVARM list, a script based on Hashin [26] was developed. The results are shown in Table 5 and compared to the experimental burst pressure reported in Kangal [15] for comparison. The burst pressure was determined when the failure index (IF) reached 1. The simulated values were all below the experimental value, relatively close to each other, except for the equivalent stress failure criterion and Hashin fibre tension mode, which was very close to the experimental value (error of 0.9 %), even closer than the numerical result reported in the referenced work (error of 3.6 %).

The experimental failure region in the study of Kangal et al. [15] refers to the cylindrical region of the COPV. The simulation here also shows failure in the cylindrical region for the equivalent stress criterion. For a 3-D visualisation of the COPV, the axisymmetric model was used as it showed the best balance between computational cost and prediction accuracy Failure occurs in the hoop layers, with stress increasing in this region due to the yield of the metal liner, a similar behaviour reported by Kangal et al. [15].

The significantly different values from the Tsai-Wu, Tsai-Hill,

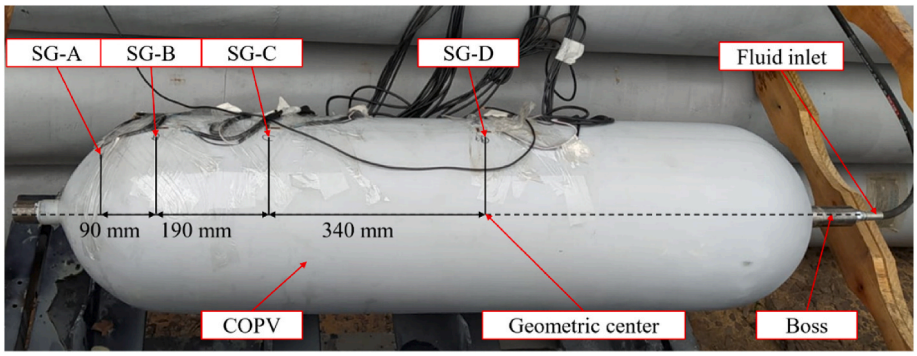

Fig. 4. The experimental burst pressure setup.

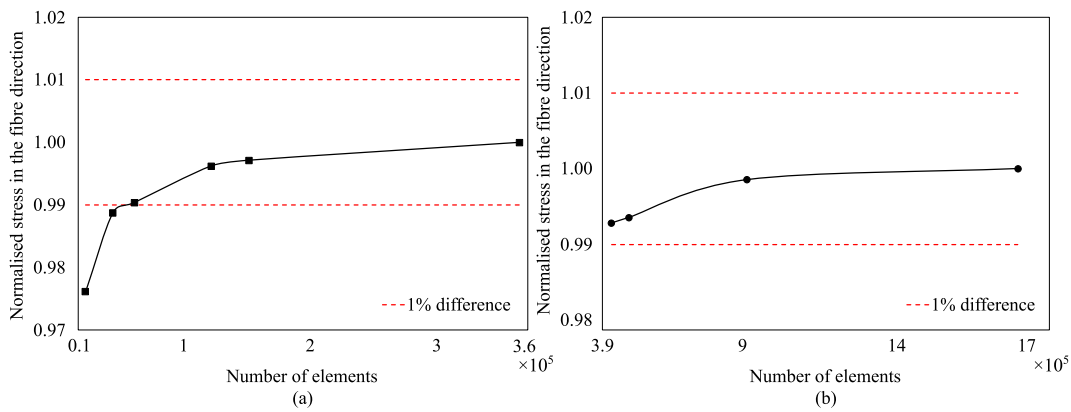

Fig. 5. Normalised stress in the fibre direction as a function of the number of elements in the meshes.

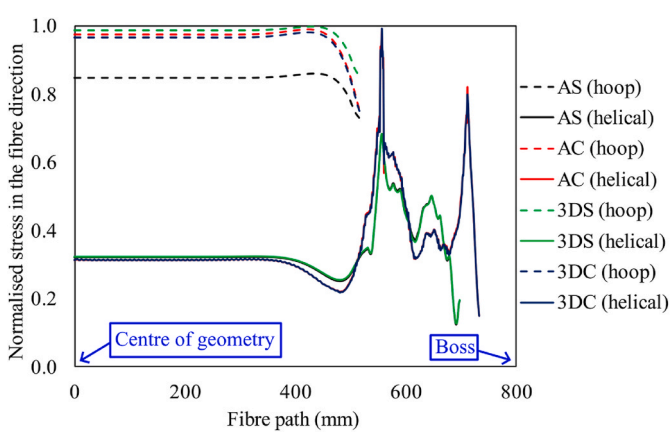

Fig. 6. Normalised stress in the fibre direction for the studied modelling approaches.

Hashin, and maximum stress failure criteria are due to the consideration of transverse stresses. The equivalent stress criterion, on the other hand, only considers tension and strength in the fibre direction. The four Hashin failure modes are presented, with the activated failure mode being matrix tension, as it shows the lowest burst pressure among them. The helical layers are subjected to higher transverse stress in the cylindrical region, leading to the initial failure since the transverse strength of the composite layer is low. Even so, in most cases, the final failure of the composite is due to the failure of the hoop layers in the fibre direction, as they are aligned with the load in the cylindrical region. As a result, the Tsai-Wu, Tsai-Hill, Hashin, and maximum stress criteria underestimate the prototype capability using first-layer failure analysis. Therefore, a simple stress analysis cannot accurately predict burst pressure, as it does not account for matrix cracking, interlaminar failure, and final fibre fracture during loading [21]. A potential alternative to increase accuracy of the numerical prediction for burst pressure is to incorporate progressive damage into the failure analysis, so that the stiffness matrix of the composite material is updated as the first layers fail. Even so, the equivalent stress criterion was also used in Sharma [6], and the numerical result for burst pressure was again close to the experimental value, with an error of 2.36 %.

4.3. Stacking sequence selection

In designing the stacking sequence of the prototype, 21 simulated models were evaluated. The selection prioritised models with the highest burst pressure, specifically those that induce failure in the cylindrical region. As described by Hu et al. [14], failure in this region is deemed safe and is marked by longitudinal failure of the hoop layers in the cylindrical region. Failure in the dome region is considered unsafe because it can cause the boss to be ejected from a project.

The burst pressure results were normalised based on the maximum burst pressure from the analyses. Fig. 8 shows the normalised burst pressure for 21 models using the equivalent stress failure criterion, which aligns closely with the burst pressure when comparing the FE model with the literature results [15]. Stacking sequences that failed in the dome region were excluded since they are considered unsafe and are therefore excluded from the design selection. The sequences exhibiting the highest burst pressures, namely Seq1, Seq2, and Seq21, were chosen.

Fig. 9a displays the burst pressures for Seq1, Seq2, and Seq21 for first ply failure from Tsai-Wu, Tsai-Hill, Hashin, and maximum stress criteria. Fig. 9b compiles the theoretical masses of the composites for each model, the mass of the liner and boss was not included because it was the same for all models. Seq1 has the lowest mass but also the lowest burst pressure, Seq2 offers higher burst pressure with intermediate mass, and

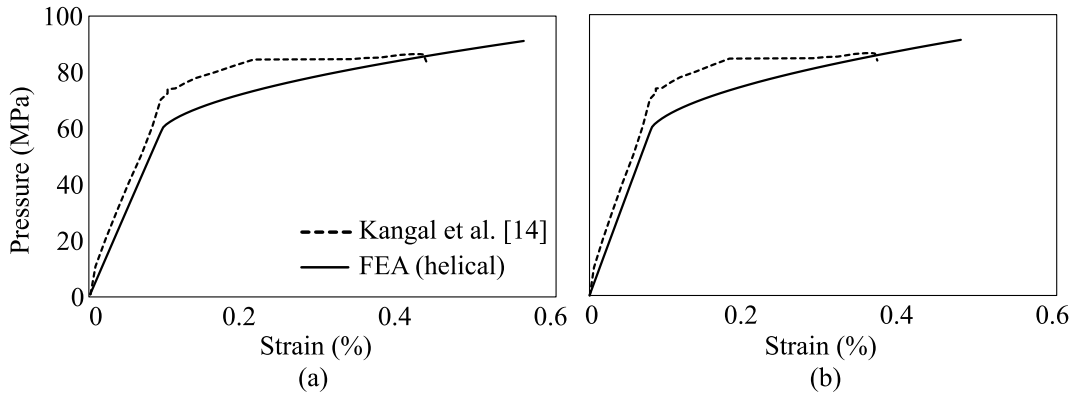

Fig. 7. Comparison of pressure versus strain data from Kangal [15] and the numerical prediction from this work in the axial (a) and hoop (b) directions.

Table 5
Comparison of estimated burst pressure, using different failure criteria, with the experimental result of Kangal et al. [15].

	Tsai-Wu	Tsai-Hill	Hashin				Max. stress	Equivalent stress	Kangal et al. [15]
			Tension		Compression				
			Matrix	Fibre	Matrix	Fibre			
Burst pressure(MPa)	37.8	37.9	36.9	87.7	62.8	73.1	37.0	91.1	91.9

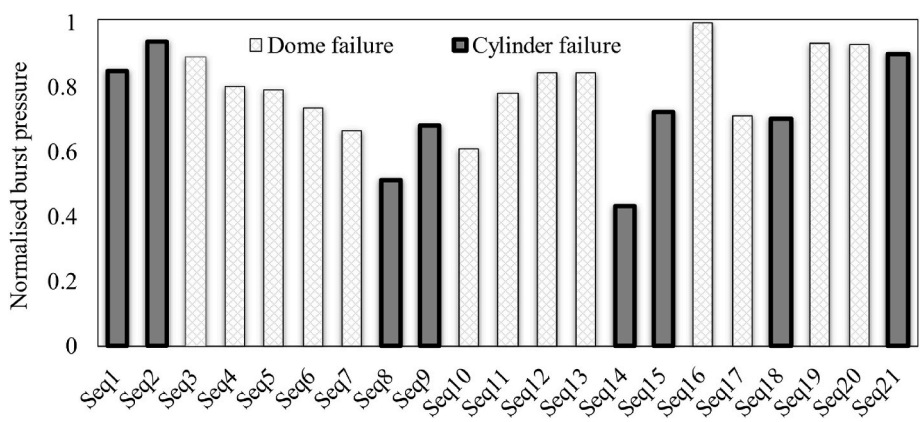

Fig. 8. Calculated burst pressures using the equivalent stress criterion for the 21 stacking sequences studied.

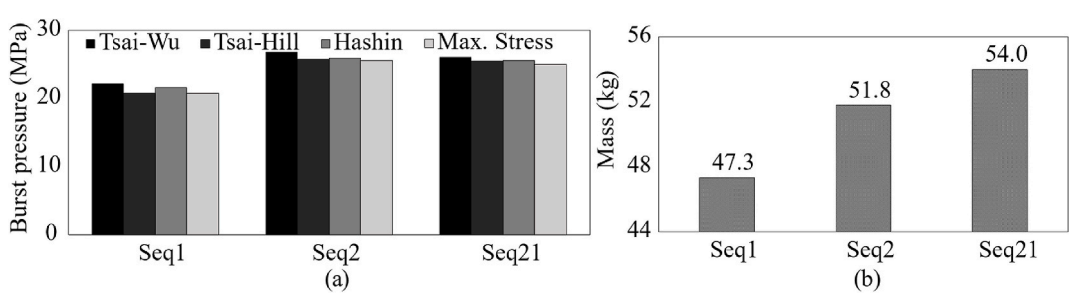

Fig. 9. Estimated burst pressure (a) and mass of the composite (b) for three stacking sequences.

Seq21 has the highest mass and intermediate burst pressure. Seq2 is deemed superior combining burst pressure and weight results. Additionally, Seq2 exhibits the largest relative difference (51 %) in burst pressure between the dome and cylinder, enhancing equipment safety, much higher than those for Seq1 and Seq21 (23 % and 30 %, respectively).

The COPV prototype following Seq2 was manufactured. Fig. 10 shows the geometric cuts made in the prototype to measure composite thickness at different regions, namely Section A-A, a dome-cylinder transition position, Section B-B, the central position of the cylinder, and the final region of the boss. The cylindrical region was 18 mm thick. Given the 49 layers of composite, the average layer thickness is 0.367 mm. This value was updated in the numerical model to perform validation with the experimental, resulting in a cylindrical region thickness of 17.98 mm. In section A-A, the model estimated a thickness of 11.50 mm, while the actual manufactured thickness was 10 mm, a 13 %

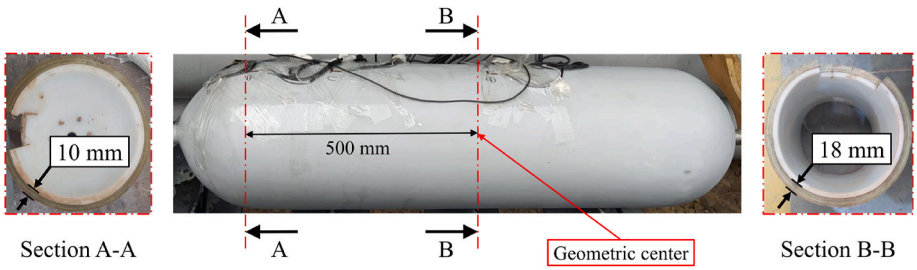

Fig. 10. Comparison of the numerical and experimental dimensions of the COPV.

difference. In the final region of the boss, the manufactured composite thickness was 30.00 mm, compared to 26.19 mm in the model, a 14.53 % difference. The mass of the manufactured composite was 44.00 kg, while the model estimated 45.68 kg, a 3.68 % difference.

For the sensitivity analysis, Seq2 incorporated angle variations as outlined in the methodology. The burst pressure was determined when the failure index (IF) reached 1. The results, shown in Fig. 11, display the normalised burst pressure for the Tsai-Wu, Tsai-Hill, Hashin, and maximum stress failure criteria. The burst pressure increases with the layer angle for Seq2_var1 and Seq2_var3 and decreases when the layer angle is reduced for Seq2_var2 and Seq2_var4. This analysis overlooks the incomplete filling in the dome area for layers at high angles. As the angle increases, the layers become more aligned with the loading direction. This alignment decreases the transverse stress in the helical layers within the cylindrical region, thereby increasing the burst pressure based on the first ply failure criteria. The Hashin criterion, particularly its matrix tensile (MT) failure index activation, indicates a predominance of transverse stresses. Therefore, an ideal stacking sequence should provide adequate coverage of the dome area and high burst pressure, as demonstrated by Seq2_ref. The variation in burst pressure is considered insignificant.

To further analyse the effect of the angle of the helical layers, Fig. 12 presents the stress in the fibre direction for an internal pressure of 20 MPa for Seq2_ref, Seq2_var1, Seq2_var2, Seq2_var3, and Seq2_var4 models. Only the most stressed helical and hoop layers of each model are included, being the first helical and hoop layers in all models. The hoop layers experience the highest stress in the cylindrical region, displaying a constant stress distribution along their length. Similar findings are reported by Hu et al. [14,23], where the hoop layers in the cylindrical region also exhibit greater tension due to their alignment with the radial loading. being vital for maintaining structural integrity in that region. Additionally, Hu et al. [14] shows that inner layers are more heavily stressed. However, in the dome-cylinder transition region, near 500 mm in length, tension in the hoop layers gradually decreases while tension in the helical layers increases.

In the dome region, the stress distribution exhibits significant oscillations along its paths, as also reported by Hu et al. [14,23]. These oscillations likely result from changes in fibre orientation due to the actual winding path in this area. An increase in the angle of helical layers helps reducing tension in the hoop layers. However, it also leads to higher stress in the helical layers and a greater stress concentration in the dome region.

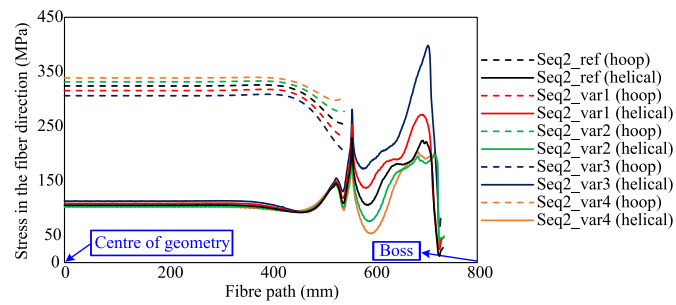

Fig. 12. Sensitivity analysis of the stacking sequence effect on stress in the fibre direction.

Fig. 13. Actual prototype after the burst test.

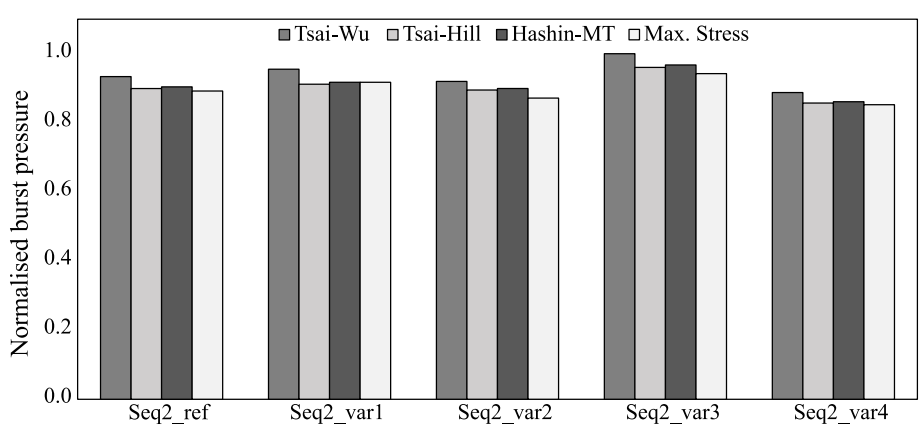

Fig. 11. Burst pressure resulting from the sensitivity analysis of the stacking sequence.

4.4. Validation of the FE model

A comparison of the burst pressure between the experiment and simulation for Seq2 was performed. Fig. 13 shows the actual prototype after the burst test, with failure near the cylindrical region, at the end of the hoop layers, agreeing with the numerical model. The numerical burst pressure obtained is 25.68 MPa, 12.62 % lower than the experimental value, 29.39 MPa. This is comparable to the values in the literature, as in Ramirez et al. [22] who reported 7.74 % using a model with progressive damage, and Hu et al. [23] who found 9.8 % using a similar approach.

The test and simulation comparison also included the analysis of strain at the 0° and 90° strain gauges. Fig. 14 displays the numerical (num.) and experimental (exp.) results for strain gauges A to D. The numerical model demonstrated higher stiffness than the manufactured COPV in both strain directions for all strain gauges, with a more pronounced difference in the dome region. This can be attributed to the type of numerical model used, since the first ply failure model does not account for progressive damage, and therefore does not reflect the decrease in structural stiffness as damage progresses. This simplification likely explains the observed differences in stiffness.

Only one burst test was performed with strain data, and more experimental tests are needed to ensure the reliability of these results. Thickness in the cylindrical region was confirmed to match the experimental setup, ruling out this factor as the source of differences in stiffness for strain gauge D. Other factors include actual lamina properties and thicknesses of individual layers due to manufacturing. Indeed, the simplification of assuming equal layer thicknesses may explain the greater differences observed in the dome region.

The greater difference in stiffness for strain gauges A, B, and C, located at the dome region, can also be attributed to this simplification. The slope of the analytical strain closely matches that of the numerical model for strain gauge D, also validating the numerical results. Using the equivalent stress criterion, the estimated analytical burst pressure is 57 MPa, higher than both the numerical and experimental values. The analytical model considers only an infinitesimal element of the cylindrical region of the COPV, approximated by a plane laminate. Since failure occurs at the end of the hoop layers, and not in the cylindrical region, the discrepancy in the analytical prediction of burst pressure is significant.

5. Conclusions

This work focused on the influence of the stacking sequence on the burst pressure of filament wound COPVs for CNG storage. The first step was to select the type of mesh to be used in the composite numerical model, observing its effect on the burst pressure. Using more elements increased simulation time, and the axisymmetric continuum mesh offered the best balance between simulation time and element count. The numerical reproduction of the COPV from Kangal et al. (2020) validated the modelling methodology, with numerical results in axial and radial directions aligning well with experimental data.

The equivalent stress criterion closely matched the experimental burst pressure, whereas other criteria underestimated it. This discrepancy is associated with the initial failure of low-angle layers of the COPV due to high transverse stresses, which reduce rigidity but do not cause immediate bursts. While composite laminate design aligns fibres with loads, the winding of type IV cylinders demands low-angle layers to suitably cover the dome region, leading to significant transverse stresses.

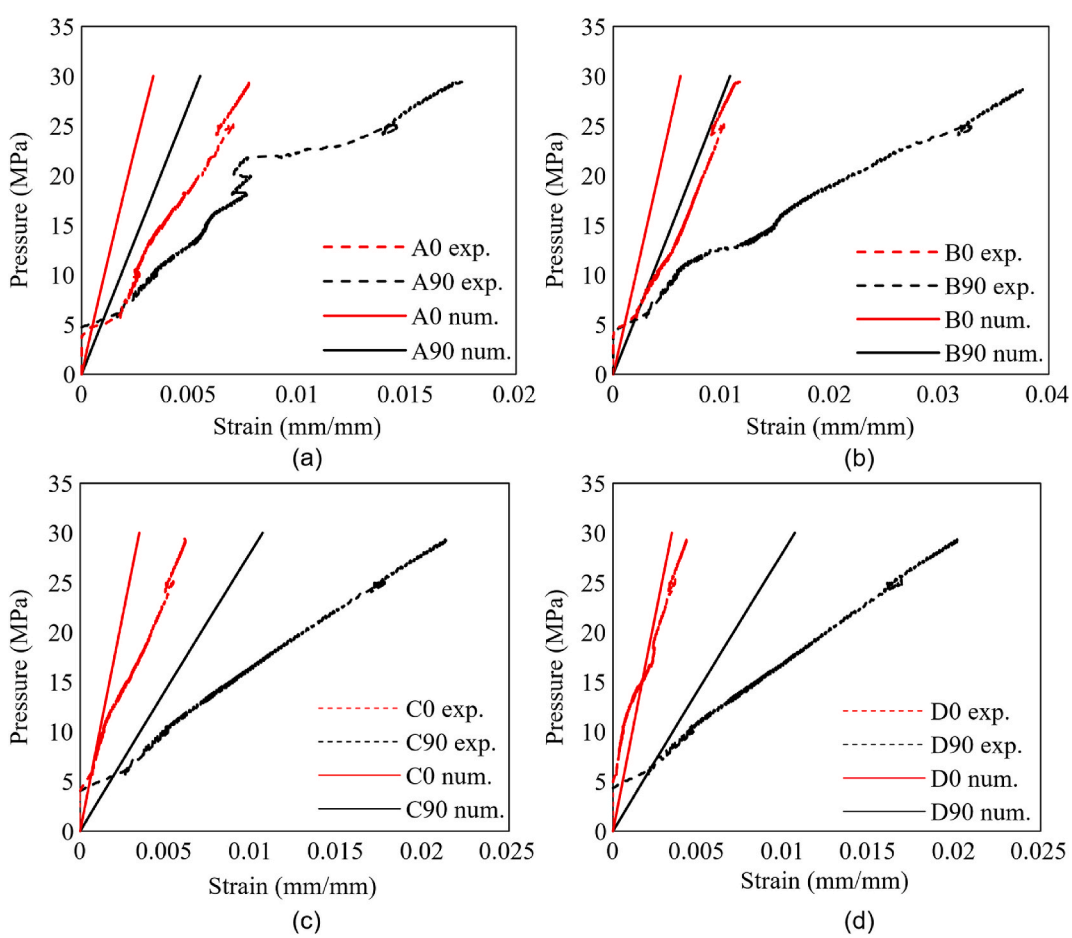

Fig. 14. Pressure vs. strain from simulations and experiments for SG-A (a), SG-B (b), SG-C (c), and SG-D (d).

The geometric comparison between the manufactured prototype and numerical model showed close alignment, with a maximum thickness difference of 14.53 % and a composite mass difference of 3.68 %. Sensitivity analysis revealed that burst pressure increases for higher angles, aligning fibre orientations with loads, and the chosen stacking sequence balanced radial and axial loads, covering the dome region effectively and yielding high burst pressure.

During the validation of the numerical model against the prototype, a 12.62% difference in burst pressure was observed, while greater discrepancies in strain were noted, attributed to model simplifications The equivalent stress criterion proved effective for initial burst pressure estimates, providing faster and more reliable results. For more accurate analysis, more complex models incorporating progressive damage into the failure analysis are necessary, as well as manufacturing and testing of additional COPVs. These represent the next steps of this research.

CRediT authorship contribution statement

Lucas L. Agne: Writing – original draft, Visualization, Software, Methodology, Investigation, Formal analysis, Data curation. **José Humberto S. Almeida Jr:** Writing – original draft, Visualization, Validation, Methodology, Investigation. **Sandro C. Amico:** Writing – review & editing, Resources, Project administration, Funding acquisition. **Maikson L.P. Tonatto:** Writing – review & editing, Supervision, Methodology, Formal analysis, Conceptualization.

Declaration of competing interest

The authors declare that they have no known competing financial interests or personal relationships that could have appeared to influence the work reported in this paper.

Data availability

Data will be made available on request.

Acknowledgements

This work was funded by FAPERGS February 2022 - Inova CLUSTERS Tecnológicos (project n° 22/2551-0000839-9). MLP Tonatto acknowledges the support from FAPERGS through the PqG Programme (project n° 24/2551-0001477-2). We also thank ISI-Polimeros for the liners and Lupatech company for manufacturing the COPVs.

Appendix I

All used material properties are presented in this appendix.

Table I.1
Material properties of the composite and liner used to validate the preliminary computational models [15].

Properties of the composite material		Values
Modulus of elasticity in direction 1	E_1 (MPa)	38500
Modulus of elasticity in direction 2	E_2 (MPa)	16500
Modulus of elasticity in direction 3	E_3 (MPa)	16500
Poisson coefficient in plane 12	ν_{12}	0.27
Poisson coefficient in plane 13	ν_{13}	0.27
Poisson coefficient in plane 23	ν_{23}	0.4
Shear modulus in plane 12	G_{12} (MPa)	4700
Shear modulus in plane 13	G_{13} (MPa)	4700
Shear modulus in plane 23	G_{23} (MPa)	4700
Tensile strength in direction 1	$(\sigma_1^T)_{ult}$ (MPa)	1250
Compressive strength in direction 1	$(\sigma_1^C)_{ult}$ (MPa)	650
Tensile strength in direction 2	$(\sigma_2^T)_{ult}$ (MPa)	36
Compressive strength in direction 2	$(\sigma_2^C)_{ult}$ (MPa)	165
Transverse shear strength	$(\tau_{12})_{ult}$ (MPa)	86
Properties of the steel liner		**Values**
Modulus of elasticity	E (MPa)	205000
Poisson coefficient	ν	0.3
Yield stress	S_y (MPa)	743

Table I.2
Material properties of the composite and liner used in the geometry and finite element parametric study [6].

Properties of the composite material		Values
Modulus of elasticity in direction 1	E_1 (MPa)	132950
Modulus of elasticity in direction 2	E_2 (MPa)	8400
Modulus of elasticity in direction 3	E_3 (MPa)	8400
Poisson coefficient in plane 12	ν_{12}	0.34
Poisson coefficient in plane 13	ν_{13}	0.34
Poisson coefficient in plane 23	ν_{23}	0.41
Shear modulus in plane 12	G_{12} (MPa)	3850
Shear modulus in plane 13	G_{13} (MPa)	3850
Shear modulus in plane 23	G_{23} (MPa)	2970
Tensile strength in direction 1	$(\sigma_1^T)_{ult}$ (MPa)	1860

(*continued on next page*)

Table I.2 (*continued*)

Properties of the composite material		Values
Compressive strength in direction 1	$(\sigma_1^C)_{ult}$ (MPa)	1470
Tensile strength in direction 2	$(\sigma_2^T)_{ult}$ (MPa)	76
Compressive strength in direction 2	$(\sigma_2^C)_{ult}$ (MPa)	85
Transverse shear strength	$(\tau_{12})_{ult}$ (MPa)	98
Properties of liner (PA6)		**Values**
Modulus of elasticity	E (MPa)	1880
Poisson coefficient	ν	0.4

Table I.3
Material properties of the composite and liner used in the converged FE models to validate experiments.

Properties of the composite material		Values
Modulus of elasticity in direction 1	E_1 (MPa)	43490
Modulus of elasticity in direction 2	E_2 (MPa)	9720
Modulus of elasticity in direction 3	E_3 (MPa)	9720
Poisson coefficient in plane 12	ν_{12}	0.267
Poisson coefficient in plane 13	ν_{13}	0.267
Poisson coefficient in plane 23	ν_{23}	0.267
Shear modulus in plane 12	G_{12} (MPa)	3106
Shear modulus in plane 13	G_{13} (MPa)	3106
Shear modulus in plane 23	G_{23} (MPa)	3106
Tensile strength in direction 1	$(\sigma_1^T)_{ult}$ (MPa)	683.97
Compressive strength in direction 1	$(\sigma_1^C)_{ult}$ (MPa)	562.6
Tensile strength in direction 2	$(\sigma_2^T)_{ult}$ (MPa)	7
Compressive strength in direction 2	$(\sigma_2^C)_{ult}$ (MPa)	74.3
Transverse shear strength	$(\tau_{12})_{ult}$ (MPa)	40.42
Properties of liner (PEAD)		**Values**
Modulus of elasticity	E (MPa)	336.762
Poisson coefficient	ν	0.46

Appendix II

In the following Table, all stacking sequences studied numerically are presented.

Table II.1
All stacking sequences used in the numerical simulations.

Name	Stacking sequence
Seq1	$[88_2/\pm10_3/88_3/\pm17_3/88_3/\pm55/88/\pm55/88_3/\pm17_3/88_3/\pm10_3/88_2]$
Seq2	$[\pm12/88/\pm12/\pm42/88_3/\pm35/\pm30/\pm23/88_3/\pm18/\pm12/88_3/\pm42/88_3/\pm35/\pm30/\pm23/88_3/\pm18_2/\pm12/88_3]$
Seq3	$[89_2/88_2/87_2/86_2/85_2/84_2/83_2/82_2/81_2/\pm40/\pm37.5/\pm35/\pm32.5/\pm30/\pm27.5/\pm25/\pm22.5/\pm20/\pm17.5/\pm15/\pm12.5]$
Seq4	$[\pm15/\pm20/\pm25/\pm30/\pm35/\pm40/\pm60/\pm80/90_{16}/\pm30/\pm15]$
Seq5	$[\pm80/\pm60/\pm40/\pm35/\pm30/\pm25/\pm20/\pm15/90_{16}/\pm12/\pm10$
Seq6	$[\pm20/\pm17.5/\pm15/\pm12.5/\pm10/\pm80/\pm60/\pm40/90_{16}/\pm12.5/\pm10]$
Seq7	$[90^\circ{}_2/\pm75^\circ/\pm65^\circ/\pm55^\circ/\pm45^\circ/\pm35^\circ/\pm25^\circ/\pm20^\circ/\pm15^\circ/\pm15^\circ/\pm20^\circ/\pm25^\circ/\pm35^\circ/\pm45^\circ/\pm55^\circ/\pm65/\pm75/90_2]$
Seq8	$[\pm12/89.5/\pm12/\pm42/89.5/\pm35/\pm30/\pm23/89.5/\pm18/\pm12/89.5/\pm42/89.5/\pm35/\pm30/\pm23/89.5/\pm18/\pm12/89.5_2]$
Seq9	$[89.5_{12}/\pm12/\pm42/\pm35/\pm30/\pm23/\pm18/\pm12/\pm42/\pm35/\pm30/\pm23/\pm18/\pm12]$
Seq10	$[90_{16}/\pm14_9]$
Seq11	$[90_2/\pm11]_9$
Seq12	$[\pm30/\pm23/\pm18/\pm12/\pm9/\pm80/\pm55/\pm42/90_{16}/\pm12/\pm9]$
Seq13	$[\pm30/\pm23/\pm18/\pm12/\pm9/\pm80/\pm55/\pm42/90_{16}/\pm12/\pm9]$
Seq14	$[90_2/\pm55/\pm42/\pm35/\pm30/\pm23/\pm18/\pm12/\pm9/\pm55/\pm42/\pm35/\pm30/\pm23/\pm18/\pm12/\pm9/90_2]$
Seq15	$[\pm16/\pm63/\pm45/90_3/\pm30/\pm25/90_3/\pm24/90_3/\pm20/90_2/\pm15.6/\pm60/\pm15.6_3/90]$
Seq16	$[89.5_2/\pm10/\pm12/\pm15/89.5_3/\pm17/\pm20/\pm25/89.5_3/\pm55/\pm63/89.5_2/\pm63/\pm55/89.5_3/\pm25/\pm20/\pm17/89.5_3/\pm15/\pm12/\pm10/89.5_2]$
Seq17	$[90_2/\pm9.43/90_3/\pm9.43/90_3/\pm9.43/90/\pm9.43/90_3/\pm9.43/90_3/\pm9.43/90_2]$
Seq18	$[\pm23/89.5/\pm15/\pm12/89.5/\pm15/\pm12/\pm42/89.5/\pm35/\pm30/\pm23/89.5/\pm18/\pm15/\pm12/89.5/\pm42/89.5_2/\pm35/\pm30/\pm23/89.5_2/\pm18/\pm15/\pm12/89.5_3]$
Seq19	$[89.5_{14}/\pm63/\pm55/\pm42/\pm30/\pm23/\pm17/\pm15/\pm12/\pm10/\pm63/\pm55/\pm42/\pm30/\pm23/\pm17/\pm15/\pm12/\pm10]$
Seq20	$[90_7/\pm63/\pm55/\pm42/\pm35/\pm30/\pm23/\pm18/\pm12/\pm9/\pm63/\pm55/\pm42/\pm35/\pm30/\pm23/\pm18/\pm12/\pm9/90_7]$
Seq21	$[\pm16/\pm63/\pm45/88_3/\pm30/\pm25/88_3/\pm24/88_3/\pm22/88_3/\pm20/88/\pm20/\pm60_2/\pm30_2/\pm15_5/88]$

References

[1] CB Azevedo, JHS Almeida Jr., HF Flores, F Eggers, SC Amico, Influence of mosaic pattern on hygrothermally-aged filament wound composite cylinders under axial compression, Journal of Composite Materials 54 (19) (2020) 2651–2659, https://doi.org/10.1177/0021998319899144.

[2] P. Blanc-Vannet, Burst pressure reduction of various thermoset composite pressure vessels after impact on the cylindrical part, Compos. Struct. 160 (Jan. 2017) 706–711, https://doi.org/10.1016/j.compstruct.2016.10.099.

[3] D. Guillon, et al., Manufacturing, burst test and modeling of high pressure thermoplastic composite overwrap pressure vessel, Compos. Struct. 316 (Jul) (2023), https://doi.org/10.1016/j.compstruct.2023.116965.

[4] E. Dahl, J.S. Becker, C. Mittelstedt, H. Schürmann, A new concept for a modular composite pressure vessel design, Compos Part A Appl Sci Manuf 124 (February) (Sep. 2019) 105475, https://doi.org/10.1016/j.compositesa.2019.105475.

[5] J.H.S. Almeida, H. Faria, A.T. Marques, S.C. Amico, Load sharing ability of the liner in type III composite pressure vessels under internal pressure, J. Reinforc. Plast. Compos. 33 (24) (2014) 2274–2286, https://doi.org/10.1177/0731684414560221.

[6] P. Sharma, P. Chugh, S. Neogi, Study to methodize the design of a safe type-4 CNG storage vessel using finite element analysis with experimental validation, Int. J. Pres. Ves. Pip. 192 (May) (2021) 104425, https://doi.org/10.1016/j.ijpvp.2021.104425.

[7] T. Angelos, Structural Design of CNG Storing Composite Pressure Vessels for Marine Applications, 2010, pp. 1–8. April 2005.

[8] N.H. Farhood, S. Karuppanan, H.H. Ya, M.A. Baharom, Burst pressure investigation of filament wound type IV composite pressure vessel, AIP Conf. Proc. 1901 (2017), https://doi.org/10.1063/1.5010482.

[9] K.R. Kashyzadeh, S.S.R. Koloor, M.O. Bidgoli, M. Petrů, A.A. Asfarjani, An optimum fatigue design of polymer composite compressed natural gas tank using hybrid finite element-response surface methods, Polymers 13 (4) (2021) 1–15, https://doi.org/10.3390/polym13040483.

[10] P. Sharma, et al., Effects of dome shape on burst and weight performance of a type-3 composite pressure vessel for storage of compressed hydrogen, Compos. Struct. 293 (April) (2022) 115732, https://doi.org/10.1016/j.compstruct.2022.115732.

[11] P. Sharma, et al., Theoretical analysis of design of filament wound type 3 composite cylinder for the storage of compressed hydrogen gas, Int. J. Hydrogen Energy 45 (46) (2020) 25386–25397, https://doi.org/10.1016/j.ijhydene.2020.06.269.

[12] M. Nebe, T.J. Asijee, C. Braun, J.M.J.F. van Campen, F. Walther, Experimental and analytical analysis on the stacking sequence of composite pressure vessels, Compos. Struct. 247 (May) (2020) 112429, https://doi.org/10.1016/j.compstruct.2020.112429.

[13] M. Nebe, A. Johman, C. Braun, J.M.J.F. van Campen, The effect of stacking sequence and circumferential ply drop locations on the mechanical response of type IV composite pressure vessels subjected to internal pressure: a numerical and experimental study, Compos. Struct. 294 (April) (2022) 115585, https://doi.org/10.1016/j.compstruct.2022.115585.

[14] Z. Hu, M. Chen, B. Pan, Simulation and burst validation of 70 MPa type IV hydrogen storage vessel with dome reinforcement, Int. J. Hydrogen Energy 46 (46) (2021) 23779–23794, https://doi.org/10.1016/j.ijhydene.2021.04.186.

[15] S. Kangal, O. Kartav, M. Tanoğlu, E. Aktaş, H.S. Artem, Investigation of interlayer hybridization effect on burst pressure performance of composite overwrapped pressure vessels with load-sharing metallic liner, J. Compos. Mater. 54 (7) (2020) 961–980, https://doi.org/10.1177/0021998319870588.

[16] I.H. Dalibor, T.V. Lisbôa, R.J. Marczak, S.C. Amico, Optimum slippage dependent, non-geodesic fiber path determination for a filament wound composite nozzle, Eur. J. Mech. Solid. 82 (Jul. 2020), https://doi.org/10.1016/j.euromechsol.2020.103994.

[17] Y. Regassa, J. Gari, H.G. Lemu, Composite overwrapped pressure vessel design optimization using numerical method, Journal of Composites Science 6 (8) (2022), https://doi.org/10.3390/jcs6080229.

[18] S. Alam, G.R. Yandek, R.C. Lee, J.M. Mabry, Design and development of a filament wound composite overwrapped pressure vessel, Composites Part C: Open Access 2 (June) (2020) 100045, https://doi.org/10.1016/j.jcomc.2020.100045.

[19] C. Liu, Y. Shi, Design optimization for filament wound cylindrical composite internal pressure vessels considering process-induced residual stresses, Compos. Struct. 235 (July 2019) (2020) 111755, https://doi.org/10.1016/j.compstruct.2019.111755.

[20] O. Kartav, S. Kangal, K. Yücetürk, M. Tanoğlu, E. Aktaş, H.S. Artem, Development and analysis of composite overwrapped pressure vessels for hydrogen storage, J. Compos. Mater. 55 (28) (2021) 4141–4155, https://doi.org/10.1177/00219983211033568.

[21] S. Lin, L. Yang, H. Xu, X. Jia, X. Yang, L. Zu, Progressive damage analysis for multiscale modelling of composite pressure vessels based on Puck failure criterion, Compos. Struct. 255 (September 2020) (2021) 113046, https://doi.org/10.1016/j.compstruct.2020.113046.

[22] J.P. Berro Ramirez, D. Halm, J.C. Grandidier, S. Villalonga, F. Nony, 700 bar type IV high pressure hydrogen storage vessel burst - simulation and experimental validation, Int. J. Hydrogen Energy 40 (38) (Oct. 2015) 13183–13192, https://doi.org/10.1016/j.ijhydene.2015.05.126.

[23] Z. Hu, et al., Investigation on failure behaviors of 70 MPa type IV carbon fiber overwound hydrogen storage vessels, Compos. Struct. 259 (May 2020) (2021) 1–11, https://doi.org/10.1016/j.compstruct.2020.113387.

[24] M. Ahmadi Jebeli, M. Heidari-Rarani, Development of Abaqus WCM plugin for progressive failure analysis of type IV composite pressure vessels based on Puck failure criterion, Eng. Fail. Anal. 131 (November 2021) (2022) 105851, https://doi.org/10.1016/j.engfailanal.2021.105851.

[25] R. Pramod, C.K. Krishnadasan, N. Siva Shanmugam, Design and finite element analysis of metal-elastomer lined composite over wrapped spherical pressure vessel, Compos. Struct. 224 (Sep) (2019), https://doi.org/10.1016/j.compstruct.2019.111028.

[26] Z. Hashin, Failure criteria for unidirectional fiber composites, Journal of Applied Mechanics, Transactions ASME 47 (2) (1980) 329–334, https://doi.org/10.1115/1.3153664.